Journal of
Materials Chemistry A

PAPER

View Article Online
View Journal | View Issue

Cite this: *J. Mater. Chem. A*, 2017, **5**, 7144

Received 12th February 2017
Accepted 15th March 2017

DOI: 10.1039/c7ta01326d

rsc.li/materials-a

Facile synthesis of ultrathin $NiCo_2S_4$ nano-petals inspired by blooming buds for high-performance supercapacitors†

Yuxiang Wen,[a] Shanglong Peng,*[a] Zilei Wang,[a] Jiaxin Hao,[a] Tianfeng Qin,[a] Shuqi Lu,[a] Jiachi Zhang,[a] Deyan He,[a] Xiaoyan Fan[c] and Guozhong Cao*[b]

3D petal-like $NiCo_2S_4$ nanostructures have been fabricated *via* a simple, mild and efficient hydrothermal strategy and the growth mechanism of $NiCo_2S_4$ nano-petals has been investigated. Such $NiCo_2S_4$ nano-petal electrodes can deliver an ultrahigh specific capacitance of 2036.5 F g^{-1} at a current density of 1 A g^{-1}, superior rate capability and remarkable cycle stability (94.3% of capacitance retention after 5000 cycles). The as-fabricated asymmetric supercapacitors based on $NiCo_2S_4$ nano-petals//active carbon electrodes demonstrate a high energy density of 35.6 W h kg^{-1} at a power density of 819.5 W kg^{-1}, with both long-term cycling and high rate stabilities. Such supercapacitors have been tested to power ten LEDs (2.03 V, 20 mA) in series for around 60 minutes, indicating their great potential for practical application.

1. Introduction

The increasingly severe global warming and the inevitability of fossil fuel depletion call for the restriction of greenhouse gas emissions as well as the exploration of eco-friendly, renewable and clean alternative energies.[1,2] At the same time, what is saliently urgent is the demand for development of energy storage and management systems for the practical application of renewable energies such as biomass, solar thermal and photovoltaic, wind, hydropower, ocean thermal, geothermal, and tidal.[3–5] Supercapacitors (SCs) have been attracting widespread interest as a very promising energy storage device with some excellent properties such as high power density, low cost, long cycle life, fast charge–discharge rate, and safe operation mode.[6–8] From a materials point of view, there are three main categories of electrode materials including carbon-based materials, transition metal oxides/hydroxides and conducting polymers.[9–12] In order to improve the performance of SCs, numerous efforts have been made to fabricate nanostructured transition metal oxides/hydroxides because they can produce much higher specific capacitances than carbon-based materials and conducting polymers.[13–18] These materials have either low conductivity or poor electrochemical stability, which greatly restricts their extensive applications in SCs.[19–21] Therefore, developing new electrode materials for desirable SC properties, such as high electrical conductivity, porous structure, high capacitance, and good electrochemical stability, is one of the urgent demands for their wide applications.

Recently, transition metal sulfides as a class of new promising active materials with high capacitance, such as CoS,[22] NiS,[23] and CuS,[24] have undergone substantial progress. Ternary nickel cobalt sulfides ($NiCo_2S_4$) have been reported to possess a much higher conductivity than their metal oxide/hydroxide counterparts, especially for $NiCo_2S_4$.[25–29] Moreover, compared to binary metal sulfides, ternary nickel cobalt sulfides achieve richer redox reactions due to the electrochemical contributions from both nickel and cobalt ions, resulting in better electrochemical performance.[30,31] Lin *et al.* studied $NiCo_2S_4$ nanosheet arrays with self-decorated nanoneedles that exhibited superior electrochemical performance when used as SC electrodes.[32] The synthesis of the $NiCo_2S_4$ nanostructures in their studies is a multistep process involving preparation of a Ni–Co precursor followed by a sulfurization treatment. Two-step solution-based hydrothermal synthesis is the most widely used approach to prepare $NiCo_2S_4$ nanostructures.[33] For example, Lu *et al.* synthesized spinel structured $NiCo_2S_4$ by sulfurizing a Ni–Co precursor with thioacetamide or sodium sulfide.[34] Hao *et al.* prepared $NiCo_2S_4$ nanotube array/carbon aerogel hybrid materials by hydrothermal growth using a Ni–Co precursor with Na_2S.[35] Shen *et al.* reported an anion exchange method to synthesize nickel cobalt sulfide ball-in-ball hollow spheres using TAA as the source of sulphur.[36] Such methods are costly and unsafe because of a complicated process under high-temperature hydrothermal or thermal conditions, which

---

[a] *Key Laboratory for Magnetism and Magnetic Materials of the Ministry of Education, School of Physical Science and Technology, Lanzhou University, Lanzhou 730000, P. R. China. E-mail: pengshl@lzu.edu.cn; Tel: +86 931 891 2753*

[b] *Department of Materials Science and Engineering, University of Washington, Seattle, Washington 98195-2120, USA. E-mail: gzcao@u.washington.edu; Tel: +1 206 616 9084*

[c] *College of Mathematics and Physics, Qingdao University of Science and Technology, Qingdao, 266061, P. R. China*

† Electronic supplementary information (ESI) available. See DOI: 10.1039/c7ta01326d

limits the large-scale production of $NiCo_2S_4$ nanostructures as electrode materials for SCs.

In this work, a facile one-step method was developed to synthesize petal-like $NiCo_2S_4$ nanostructures by a hydrothermal process. Such $NiCo_2S_4$ nano-petals as an electrode in asymmetric supercapacitors (ASCs) show an ultrahigh specific capacitance of 2036.5 F g^{-1} at a current density of 1 A g^{-1}, superior rate capability and remarkable cycle stability (94.3% capacitance retention after 5000 cycles). The as-fabricated asymmetric supercapacitor presents a high energy density of at 35.6 W h kg^{-1} at a power density of 819.5 W kg^{-1}, as well as robust long-term cycling stability, indicating a promising practical application.

2. Experimental sections

All the reagents used in the experiment are of analytical grade without further purification.

2.1 Synthesis of the $NiCo_2S_4$ NPs

Prior to the synthesis, a piece of Ni foam (NF) was carefully cleaned through sonication consecutively in 3 M HCl, acetone, ethanol and deionized (DI) water (20 min each) to remove the surface oxidized layer and other impurities. The fabrication process of the $NiCo_2S_4$ NPs is shown in Fig. 1. In a typical one-step hydrothermal procedure for preparing $NiCo_2S_4$ samples, the ratio of $Ni(NO_3)_2\cdot 6H_2O : Co(NO_3)_2\cdot 6H_2O :$ thiourea was kept the same as 1 : 2 : 4 for each sample, while the concentration of $Ni(NO_3)_2\cdot 6H_2O$ is varied from 1 M to 12 M. First, they were entirely dissolved into 40 ml of H_2O/ethylene glycol solvent (1 : 1 by volume) with magnetic stirring for 30 min to form a pink solution. Subsequently, the surface-cleaned NF was immersed into the solution, and it was then transferred to an electric oven and maintained at 90 °C for 12 hours. When cooled down to room temperature naturally, the samples were fetched out and washed several times with DI water and ethanol to remove any unreacted residues. Finally, the samples were dried at 80 °C overnight. The obtained $NiCo_2S_4$ samples are denoted as H-$NiCo_2S_4$-n (n = 1, 2, 6, 8, 10 and 12) and the sample (n = 4) is henceforth expressly referred to as H-$NiCo_2S_4$ without specific instructions. The mass loading of active materials can be estimated by the mass difference of the Ni foam before and after reaction. The typical mass loading of the H-$NiCo_2S_4$ is about 0.91 mg cm^{-2}. For comparison, an E-$NiCo_2S_4$ sample coated on NF was obtained by electrochemical deposition by cyclic voltammetry with a minor change of using nitrates instead of chlorates according to the previously reported method.[37] Also, E-$NiCo_2S_4$ samples were prepared with various cycle numbers from 10 to 45 cycles. The mass loading of the E-$NiCo_2S_4$ sample (15 cycles) is about 0.85 mg cm^{-2}.

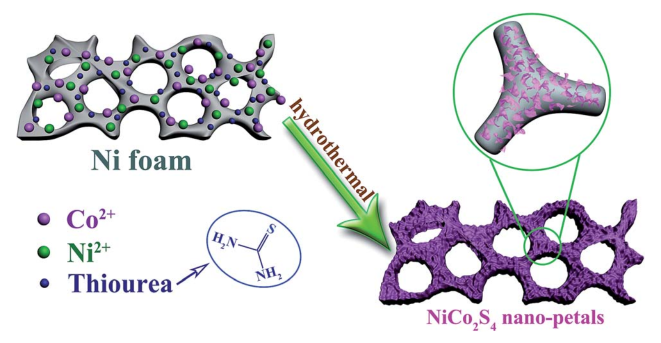

Fig. 1 Schematic illustration of the fabrication process for the $NiCo_2S_4$ nano-petals grown on Ni foam.

2.2 Fabrication and assembly of $NiCo_2S_4$//AC asymmetric supercapacitors (ASCs)

The fabrication of the $NiCo_2S_4$//AC ASCs was conducted by taking the $NiCo_2S_4$ NPs and active carbon as the positive and negative electrodes, respectively. 1 M KOH solution was used as the electrolyte, and a porous filter paper as the separator. The negative electrode was prepared by mixing AC, acetylene black and polyvinylidene fluoride (PVDF) with a mass ratio of 8 : 1 : 1 to form a homogeneous slurry, which was uniformly coated onto a Ni foam substrate. The negative electrode was pressed and then dried under vacuum at 80 °C for 12 hours. The asymmetric supercapacitors were carefully assembled and sealed by insulated rubber tape and sealing tape to avoid evaporation of the aqueous electrolyte during long-term measurements. Prior to the fabrication of the asymmetric supercapacitors, the masses of the positive and negative electrodes were balanced according to the following equation:[37]

$$\frac{m_+}{m_-} = \frac{C_{s-}\Delta V_-}{C_{s+}\Delta V_+}$$

where m is the mass, C_s the specific capacitance of a single electrode at a scan rate of 30 mV s^{-1}, and ΔV the voltage range for positive (+) and negative (−) electrodes. The typical mass loading of H-$NiCo_2S_4$//AC and E-$NiCo_2S_4$//AC ASCs was about 3.69 mg cm^{-2} and 2.83 mg cm^{-2}, respectively.

2.3 Materials characterization

The microstructure and morphology were investigated by using field emission scanning electron microscope microscopy (FE-SEM, Hitachi S-4800) and transmission electron microscopy (TEM, FEI Tecnai G2 F30 microscope operated at 300 kV). XRD measurements were performed on a Rigaku D/MAX-2400 X-ray diffractometer using Cu Kα radiation (λ = 0.154056 nm). The chemical component was analysed on a micro-Raman spectroscope (JY-HR800, 532 nm wavelength YAG laser) and a multifunctional X-ray photoelectron spectroscope (PHI-5702, Mg KR X-ray, 1253.6 eV).

2.4 Electrochemical measurements

The electrochemical tests were carried out at room temperature in both three-electrode and two-electrode configurations. In the three-electrode measurements, the $NiCo_2S_4$ NPs on Ni foam electrode was used as the working electrode, a Pt plate as the counter electrode, and Hg/HgO as the reference electrode. In the two-electrode measurements, the asymmetric supercapacitors were assembled with $NiCo_2S_4$ acting as the positive electrode and active carbon as the negative electrode. 1 M KOH solution served as the electrolyte for all electrochemical measurements. The electrochemical performance was tested on an electrochemical workstation (CHI660E, CH Instrument In, Shanghai) by the techniques of electrochemical impedance spectroscopy (EIS), cyclic voltammetry (CV), and galvanostatic charge–discharge (GCD). The voltage window is from −0.2 to 0.6 V *vs.* Hg/HgO for the positive $NiCo_2S_4$ electrode, −1.0 to 0 V *vs.* Hg/HgO for the negative AC electrode, and thus 0 to 1.6 V for the asymmetric $NiCo_2S_4$//AC supercapacitors.

The capacitance values were calculated from the galvanostatic charge–discharge curves according to the following equations:

For single electrodes,

$$C_s = \frac{I\Delta t}{mV}$$

For ASCs,

$$C_{ASC} = \frac{I\Delta t}{MV}$$

where the specific capacitance (C_s) applies to a single electrode and the ASC capacitance (*C*ASC) applies to the two-electrode only, and *I*, Δt and *V* are the discharging current, discharging time and voltage change, respectively. *m* is the mass of the electroactive materials on the single electrodes, and *M* the total mass of the electroactive materials based on both the positive and negative electrodes ($M = m_+ + m_-$).

The calculation of energy and power density is based on the total weight of the two electrodes in the ASCs according to the following equations:

$$E = \frac{C_{ASC}V^2}{2}$$

$$P = \frac{E}{\Delta t} = \frac{C_{ASC}V^2}{2\Delta t}$$

where *E* is the energy density, *P* the power density, *C*ASC the ASCS capacitance, *V* the maximum voltage change, and Δt the discharge time.

3. Results and discussion

Fig. 2 shows the SEM images of the as-synthesized H-$NiCo_2S_4$ nano-petals on NF. As shown in Fig. 2a and S1,† the H-$NiCo_2S_4$ nano-petals are firmly grown on NF while maintaining the 3D macroporous structure of the NF, which are dense yet homogeneous. As shown in Fig. 2b for the high magnification SEM, the interconnected H-$NiCo_2S_4$ nano-petals with large diameters and an ultrathin thickness of 7.6–30 nm are vertically grown on the NF substrate, forming a highly porous architecture. Such an open structure is beneficial to the effective electron transport at the electrode/electrolyte interface.[38] Fig. S2a† presents a microscopic overview of E-$NiCo_2S_4$ nanosheets with a highly uniform distribution on NF, which is generally similar to the H-$NiCo_2S_4$ ones. However, it can be observed that the E-$NiCo_2S_4$ nanosheets have a smaller size than H-$NiCo_2S_4$ nano-petals in Fig. S2b.† Fig. 2c, d and S3† exhibit the EDX mapping images of the elements Ni, Co, and S in the $NiCo_2S_4$ samples. The even distribution of the Ni, Co and S elements demonstrates the uniform growth of the $NiCo_2S_4$ nano-petals and nanosheets, which further indicates the successful preparation of the $NiCo_2S_4$ samples by one-step hydrothermal and electrodeposited processes. Herein, the nickel element content is the highest because the nickel element exists in both $NiCo_2S_4$ and NF.

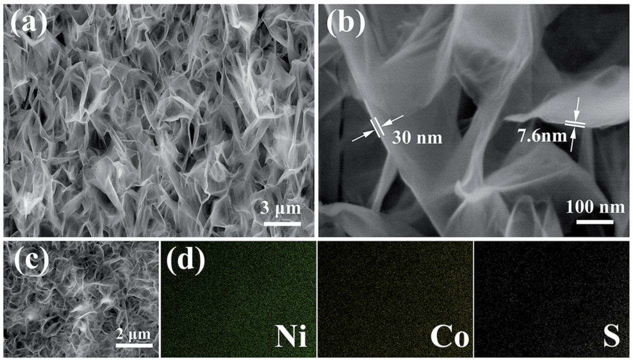

Fig. 2 (a and b) SEM images of H-$NiCo_2S_4$, (c) the SEM image of the region for elemental mapping, and (d) Ni, Co, and S element mapping based on image (c).

TEM was used to further probe the structure of the H-$NiCo_2S_4$ nano-petals obtained by violent ultrasonication from NF, as shown in Fig. 3a and S4a.† It can be observed that the cross-linking nano-petals with ultrathin thickness are in accordance with the SEM image as shown in Fig. 2b. This structure can take full advantage of the electroactive sites within H-$NiCo_2S_4$ nano-petals. TEM images in Fig. S4c† reveal the morphology of E-$NiCo_2S_4$ nanosheets. Laminating nanosheets in the field of view confirmed a smaller size relative to H-$NiCo_2S_4$ nano-petals. The "graphene-like" structure of H-$NiCo_2S_4$ with oversized and ultrathin nano-petals can provide a large specific surface area which is

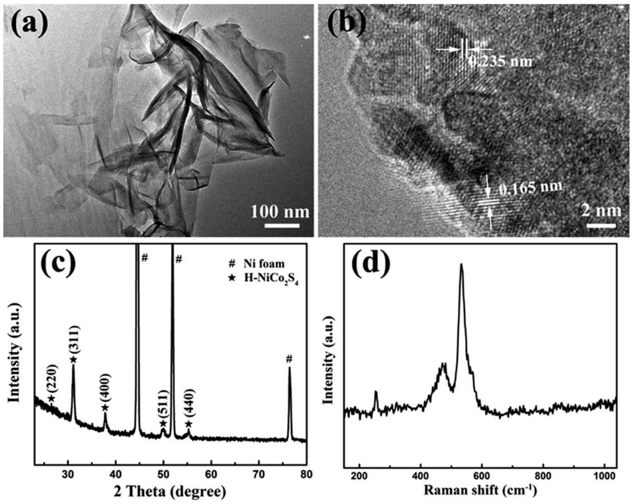

Fig. 3 (a) TEM and (b) HRTEM images of the H-$NiCo_2S_4$ nano-petals. (c) XRD pattern and (d) Raman spectra of the H-$NiCo_2S_4$ nano-petals.

conducive to the diffusion of electrolyte ions and the transfer of electrons, thereby improving the electrochemical performance of supercapacitors.[19] The selected area electron diffraction (SAED) pattern recorded from the nano-petals is shown in Fig. S4b,† which represents continuous diffraction rings revealing the polycrystalline nature of H-$NiCo_2S_4$ nano-petals. A high-resolution TEM (HRTEM) image (Fig. 3b) displays two obvious crystal lattices corresponding to the (400) and (440) crystal planes of the $NiCo_2S_4$ phase. Similarly, the fringe spacing based on E-$NiCo_2S_4$ in Fig. S4d† coincides well with the interlayer spacing of the (422) and (400) planes of cubic $NiCo_2S_4$. Fig. 3c shows X-ray diffraction (XRD) patterns of the H-$NiCo_2S_4$ sample on NF. The marked peaks at 26.6°, 31.2°, 37.8°, 50.0° and 55.3°, correspond to the (220), (311), (400), (511), and (440) planes of the cubic phase of $NiCo_2S_4$ (JCPDS card no. 20-0782), respectively. The XRD results are in good agreement with the HRTEM results and support the above-mentioned conclusion that the nano-petals are pure $NiCo_2S_4$. These results are also confirmed by the Raman spectra of the H-$NiCo_2S_4$ sample as shown in Fig. 3d. It can be clearly seen that there are three distinct peaks at 252.7, 471.1 and 531.9 cm^{-1}, corresponding to F_{2g}, F_{2g} and E_g models of $NiCo_2S_4$, respectively.[39]

The elemental composition and chemical state of H-$NiCo_2S_4$ samples were analyzed by XPS in the near-surface region as shown in Fig. 4. Fig. 4a presents the survey spectrum of H-$NiCo_2S_4$. The peaks in the spectrum correspond to elements Ni, Co, S, C, and O. The element O may come from absorbed CO_2 in air, and the element C is from the reference carbon.[40] The Co 2p and Ni 2p spectra were fitted by a Gaussian fitting method considering two spin–orbit doublets and two shake-up satellites. As revealed in Fig. 4b, two kinds of cobalt species containing Co^{3+} and Co^{2+} can be observed. The binding energies at around 777.2 and 796.9 eV of the Co 2p peaks indicate the existence of Co^{3+}, while the binding energies at 782.5 and 798.0 eV are characteristic of Co^{2+}. The weak satellite peaks indicate that the majority of Co element was in the Co^{3+} state.[40] As depicted in Fig. 4c, the fitting Ni 2p peaks at 856.1 and 873.2 eV correspond to Ni^{2+}, and the fitting Ni 2p peaks at 858.2 eV and 874.7 eV are indexed to Ni^{3+}. The intense Sat. peaks suggest that Ni^{2+} is the major state for element Ni.[38] Similarly for the S 2p region in Fig. 4d, the component at 163.1 eV (S $2p_{1/2}$) is associated with the binding energies of metal–sulfur bonding (Ni–S and Co–S bonding), while the component at 161.8 eV ($2p_{3/2}$) is attributed to the presence of sulfur ions in a low coordination state at the surface.[30,33] Based on the above XPS results, the H-$NiCo_2S_4$ is composed of Co^{2+}, Co^{3+}, Ni^{2+}, Ni^{3+} and S^{2-}. These results are in good agreement with other reported data for the chemical states of $NiCo_2S_4$.[27,30,41,42] Also, the chemical states of E-$NiCo_2S_4$ were investigated by means of XPS and the results are shown in Fig. S5.† The survey spectrum of E-$NiCo_2S_4$ (Fig. S5a†) bears a remarkably close resemblance to that of H-$NiCo_2S_4$. The peaks of elements Ni, Co, S, C, and O in the spectrum are in accordance with those of H-$NiCo_2S_4$. With regard to the Co 2p spectrum, the binding energies located at 781.7 and 798.0 eV are assigned to Co^{2+}, and the binding energy situated at 777.3 eV and 796.3 eV are ascribed to Co^{3+}. Likewise, the Ni 2p XPS spectrum was best fitted with two spin–orbit doublets: one at 853.9 and 872.8 eV and the other at 857.3 and 874.8 eV, corresponding to Ni^{2+} and Ni^{3+}, respectively. The binding energies centered at 163.1 and 161.7 eV are related to the S $2p_{1/2}$ and S $2p_{3/2}$, respectively. These results indicate that the H-$NiCo_2S_4$ and E-$NiCo_2S_4$ fabricated by two distinct methods possess essentially the same elemental composition and chemical state.

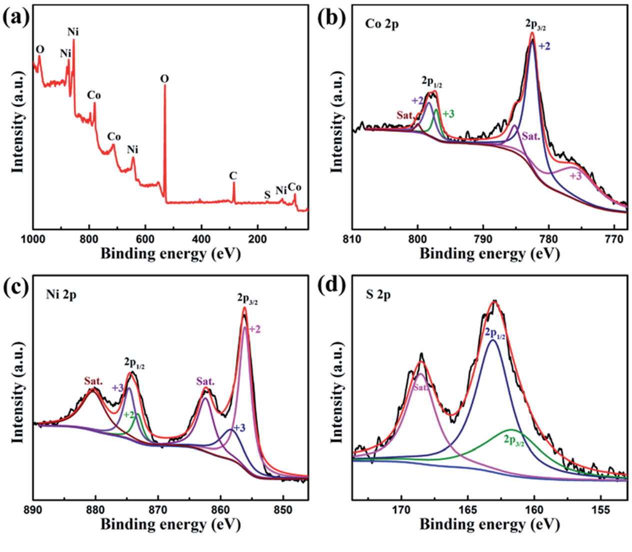

Fig. 4 (a) XPS spectra of survey, (b) Co 2p, (c) Ni 2p, and (d) S 2p for the H-$NiCo_2S_4$ samples (Sat. means shake-up satellites).

To gain insight into the growth mechanism of the H-$NiCo_2S_4$ nano-petals, a series of control samples were fabricated by altering the solution concentration while maintaining a constant temperature and time. As shown in Fig. 5a, the H-$NiCo_2S_4$-1 sample exhibits a few bud-like micro-particles with a diameter of about 1–3 μm; the petal-like nanostructure with a low magnitude size can also be observed in the inset of Fig. 5a. Subsequently, the micro-particles gradually melted into nanoparticles, and the nano-petals came out along with the increase of solution concentration as shown in Fig. 5b. Then the nanoparticles on the top of the NPs entirely disappeared until $n = 4$ as described in Fig. 5c, forming highly uniform distribution on NF. In light of the observations, the bud-like nanoparticles/micro-particles with gradually expanding diameters appeared again with increasing the solution concentration in multiples from $n = 6$ to 12 as demonstrated in Fig. 5d–g. From the above, the growth process of the H-$NiCo_2S_4$ nano-petals can be described as the process of flowers in full bloom, as shown in Fig. 6. First, the cations (Ni^{2+}, Co^{2+}) and anions (S^{2-}) from the reaction solution formed micro-granular $NiCo_2S_4$ buds through a nucleation process,[13,43] accompanied by a tiny bit of dissolution. Then, $NiCo_2S_4$ buds gradually blossomed to form a uniform and dense H-$NiCo_2S_4$ petal with the increase of the reaction time. Fig. 5h shows the EDS mapping results of Ni, Co and S elements based on the TEM image of a "bud" in Fig. 5g. Apparently, it can be observed that the content of Ni, Co and S elements in the "bud" is higher than that in the surrounding NPs, which confirms the formation mechanism of the NPs as stated above. In order to further verify the analysis, the reaction

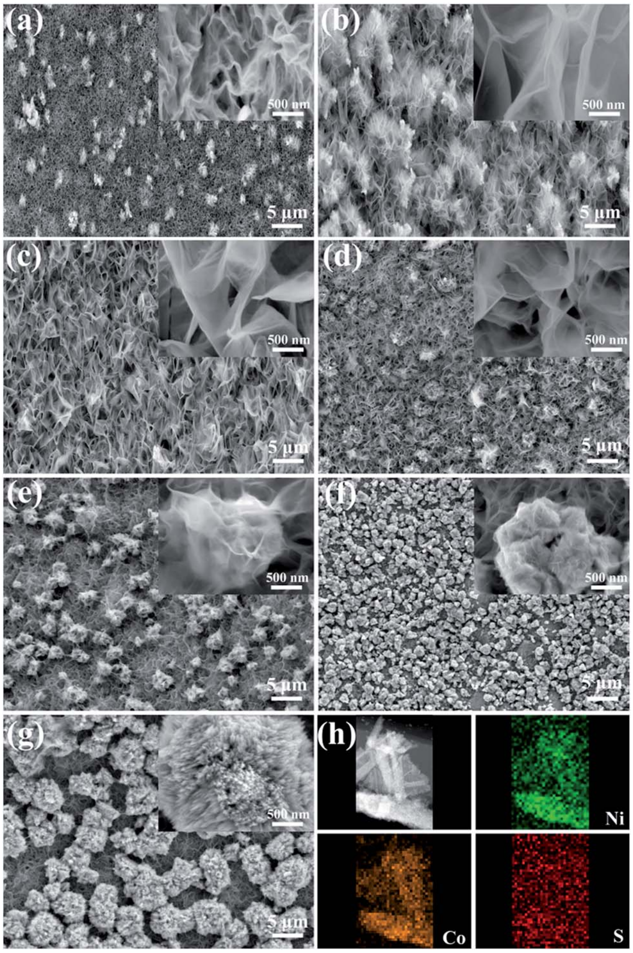

Fig. 5 SEM images of H-$NiCo_2S_4$-n nanostructures synthesized by a one-step facile hydrothermal method with different solution concentrations at 90 °C for 12 h: (a) $n = 1$, (b) $n = 2$, (c) $n = 4$, (d) $n = 6$, (e) $n = 8$, (f) $n = 10$ and (g) $n = 12$. (h) The EDS mapping results of Ni, Co, and S elements based on the TEM image of a "bud" in (g).

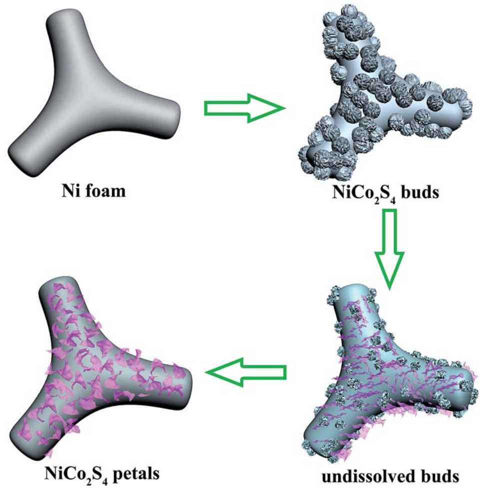

Fig. 6 Schematic illustration of the blooming process of H-$NiCo_2S_4$ "buds".

time of H-$NiCo_2S_4$-n ($n = 10, 12$) was extended to 24 h. After that, the undissolved $NiCo_2S_4$ buds are all in full bloom (Fig. S6†), exhibiting an extremely similar morphology to that of H-$NiCo_2S_4$. Nevertheless, the process is time consuming contrary to the original intention of a simple, facile and efficient design approach for large-scale application. Thus, the H-$NiCo_2S_4$ NPs were chosen for the following electrochemical performance tests. Similarly, we explored the growth of the E-$NiCo_2S_4$ nanosheets by adjusting the cycle numbers during the process of electrodeposition. As shown in Fig. S7,† with the increase of the cycle number, the obtained E-$NiCo_2S_4$ nanosheets transform from lightly deposited nanosheets (Fig. S7a†), to moderately deposited nanosheets (Fig. S2a†), and then to heavily deposited nanosheets (Fig. S7c†) with some cracks due to their mechanical expansion, and finally to excessively deposited nanospheres composed of oversized nanosheets though stacks and agglomeration.

The electrochemical performances of the as-synthesized samples as a positive electrode were investigated in a three-electrode configuration. For comparison, the E-$NiCo_2S_4$ nanosheet electrode was also tested under the same conditions as the H-$NiCo_2S_4$ electrode. Fig. 7a and b show the CV curves of the H-$NiCo_2S_4$ and E-$NiCo_2S_4$ electrodes at different scan rates ranging from 5 to 100 mV s^{-1}, respectively. The obvious redox reaction peaks in the CV curves indicate distinct pseudocapacitive characteristics of the electrode materials, which are from reversible faradaic redox processes of Ni^{2+}/Ni^{3+} and Co^{2+}/Co^{3+} transitions associated with OH^- anions, as illustrated by the following equations:[35]

$$\mathrm{CoS + OH^- \rightleftarrows CoSOH + e^-}$$

$$\mathrm{CoSOH + OH^- \rightleftarrows CoSO + H_2O + e^-}$$

$$\mathrm{NiS + OH^- \rightleftarrows NiSOH + e^-}$$

From the CV curves of the H-$NiCo_2S_4$ samples in Fig. 7a, two pairs of well-defined redox peaks can be observed. In particular,

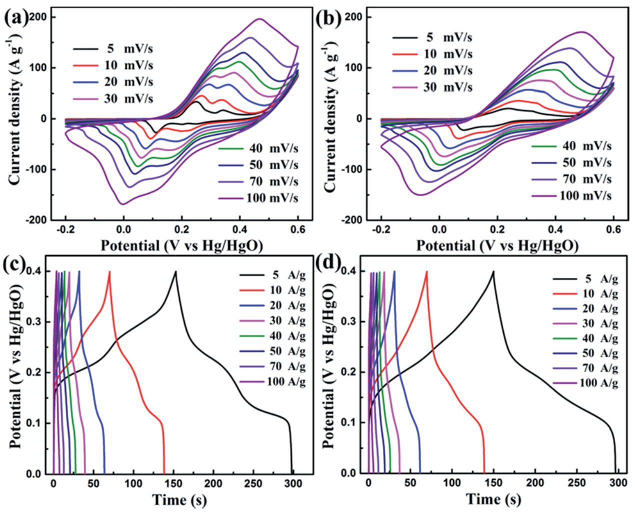

Fig. 7 CV curves of the (a) H-$NiCo_2S_4$ and (b) E-$NiCo_2S_4$ electrodes measured at different scan rates. GCD curves of the (c) H-$NiCo_2S_4$ and (d) E-$NiCo_2S_4$ electrodes obtained at various current densities.

the first pair of redox peaks in CV curves might be attributed to faradaic reactions to produce NiSOH and CoSOH, while the second pair near to a more positive potential might be from the redox reaction between CoSO and CoSOH.[44] With the increase of scan rates, the current density gradually increases. The anodic peaks shift to the positive direction, and the cathodic peaks shift to the negative direction, indicating a relatively low resistance and fast redox reactions of the $NiCo_2S_4$ electrodes.[45] For comparison, the CV curves of the H-$NiCo_2S_4$ and E-$NiCo_2S_4$ electrodes at the same scan rate of 100 mV s^{-1} are shown in Fig. 8a. It is noteworthy that the CV curves still show the obvious redox peaks at such a large scan rate, revealing that the nanopetal/nanosheet structures are beneficial to fast redox reactions. In addition, the integrated CV area of the H-$NiCo_2S_4$ electrode is a little larger than that of the E-$NiCo_2S_4$ electrode, suggesting that the ultrathin H-$NiCo_2S_4$ nano-petals can provide a convenient and fast electron/ion-transport path. As shown in Fig. 7c and d, the GCD curves show symmetric charge and discharge processes at various current densities ranging from 5 to 100 A g^{-1}, indicating good pseudocapacitive features and excellent reversibility. Specifically, two discharging platforms are clearly displayed in the GCD curves of the H-$NiCo_2S_4$ electrodes, which is in good agreement with the two pairs of redox peaks in Fig. 7a. Fig. S8a† shows the effects of solution concentration on the mass loading and specific capacitance of the H-$NiCo_2S_4$-*n* electrodes. The H-$NiCo_2S_4$ electrodes reveal the largest mass loading of active materials and moderate specific capacitance at the current density of 1 A g^{-1} compared with the other H-$NiCo_2S_4$-*n* samples. Also, the H-$NiCo_2S_4$ displays an excellent rate performance as depicted in Fig. S8b,† which still retains about 83.6% of the initial capacitance when the current density increases to a large current density of 100 A g^{-1}.

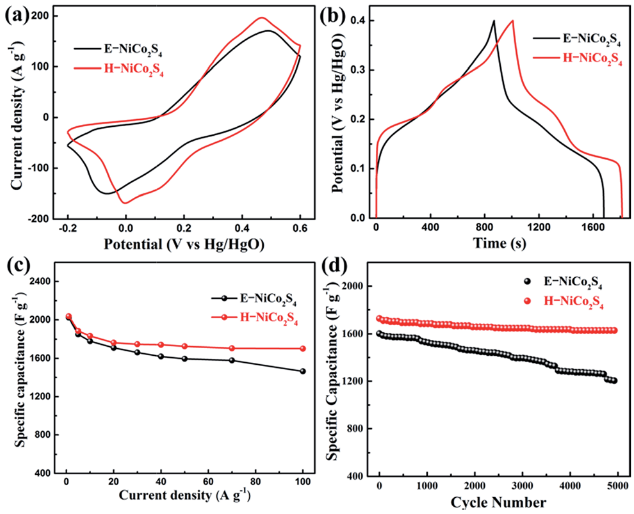

Fig. 8 (a) Comparison of the CV curves of the H-$NiCo_2S_4$ and E-$NiCo_2S_4$ electrodes at 100 mV s^{-1}. (b) GCD curves of the H-$NiCo_2S_4$ and E-$NiCo_2S_4$ electrodes obtained at 1 A g^{-1}. (c) The specific capacitance as a function of current density for the H-$NiCo_2S_4$ and E-$NiCo_2S_4$ electrodes. (d) Cycling performance of the prepared H-$NiCo_2S_4$ and E-$NiCo_2S_4$ electrodes during 5000 cycles at a constant current density of 50 A g^{-1}.

Likewise, Fig. S8c and d† show the electrochemical properties of E-$NiCo_2S_4$ samples prepared with different cycle numbers. The E-$NiCo_2S_4$ sample fabricated with 15 cycles exhibits the highest specific capacitance and the optimal rate performance. Moreover, the mass loading of active materials increases with the increase of the cycle number, which is in accordance with the principle of electrochemical deposition.

Fig. 8b shows the GCD curves of the H-$NiCo_2S_4$ and E-$NiCo_2S_4$ electrodes at the current density of 1 A g^{-1}. The H-$NiCo_2S_4$ electrodes deliver higher capacitance than the E-$NiCo_2S_4$ electrode due to longer discharging time. Rate capability is one of the crucial parameters for supercapacitors. Thus, the calculated specific capacitances based on the discharge curves as a function of the current density are plotted in Fig. 8c. The specific capacitances of the H-$NiCo_2S_4$ electrode are 2036.5, 1886.1, 1834.2, 1763.6, 1747.7, 1742.6, 1726.0 and 1705.5 F g^{-1} at the current densities of 1, 5, 10, 20, 30, 40, 50 and 70 A g^{-1}, respectively. Even at a large current density of 100 A g^{-1}, it still remains at 1701.8 F g^{-1}, exhibiting incredible rate capability and remarkable electrochemical capacitance. The specific capacitances of the E-$NiCo_2S_4$ electrodes are 2023.1 F g^{-1} and 1464.4 F g^{-1} at the current densities of 1 and 100 A g^{-1}, respectively. Apparently, with the increase of current density, the specific capacitance retention of 72.4% for the E-$NiCo_2S_4$ electrodes is lower than that of 83.6% for the H-$NiCo_2S_4$, which can be attributed to the better electronic conductivity revealed by EIS measurements as shown in Fig. S9.† The Nyquist plot in Fig. S9† shows that the H-$NiCo_2S_4$ electrodes present a lower R_c (a combined resistance containing ionic resistance for the electrolyte, intrinsic resistance of the substrate, and contact resistance at the active material/current collector interface)[46] of 1.24 Ω than the E-$NiCo_2S_4$ electrodes (1.40 Ω) in a high frequency range, indicating better electrical conductivity. The two electrodes show a more than 70° sloped line in the low frequency region, which implies their typical capacitor behavior. Fig. 8d presents the excellent cycling stability of the $NiCo_2S_4$ electrodes at a charge/discharge current density of 100 A g^{-1} for 5000 cycles. 74.9% of the initial specific capacitance for the E-$NiCo_2S_4$ electrodes and 94.3% of the initial specific capacitance for the H-$NiCo_2S_4$ electrodes were retained after 5000 cycles.

To further investigate the energy storage performance of the H-$NiCo_2S_4$ and E-$NiCo_2S_4$ electrodes for practical applications, two asymmetric supercapacitors were successfully assembled using H/E-$NiCo_2S_4$ as the positive electrode and AC as the negative electrode (Fig. 9a). Fig. 9b shows the individual CV curves of the positive and negative electrodes at a scan rate of 30 mV s^{-1} in a voltage range from −1 to 0 V and −0.2 to 0.6 V, respectively, implying 1.6 V or more of the working voltage for the assembled ASCs. Fig. S10a and b† present the CV and GCD curves of AC. The specific capacitances of AC at various current densities are shown in Fig. S10c.† The mass ratios of H-$NiCo_2S_4$/E-$NiCo_2S_4$ to AC were controlled to be about 1 : 4/1 : 3.3 in ASCs according to the principle of charge balance of the electrodes (see the Experiment section). Fig. S11a and b† exhibit the CV curves of the H-$NiCo_2S_4$//AC and E-$NiCo_2S_4$//AC ASCs at different operation voltages varying from 0–1.0 to 0–1.8 V at the

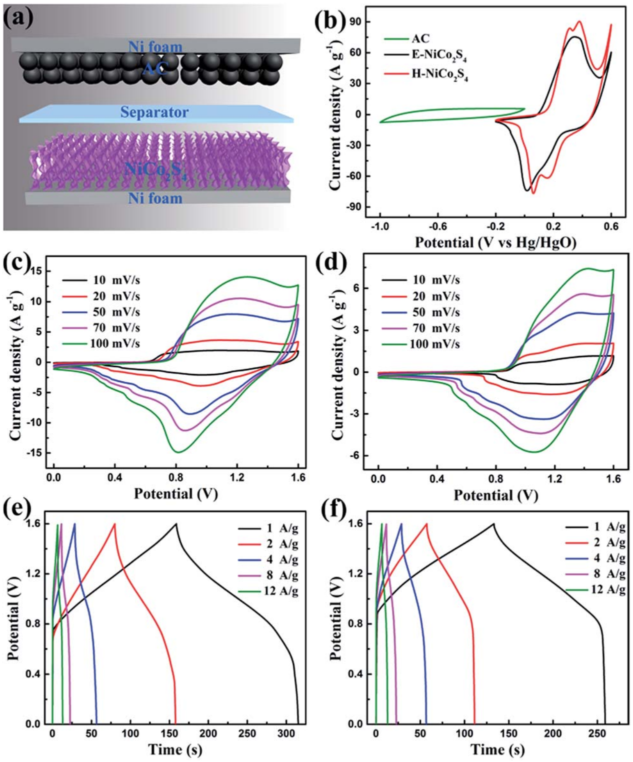

Fig. 9 (a) Schematic illustration of the assembled asymmetric supercapacitors. (b) CV curves of the H-$NiCo_2S_4$, E-$NiCo_2S_4$ and AC electrodes at a scan rate of 30 mV s^{-1}. CV curves of the (c) H-$NiCo_2S_4$//AC and (d) E-$NiCo_2S_4$//AC ASCs at scan rates of 10–100 mV s^{-1}. GCD curves of the (e) H-$NiCo_2S_4$//AC and (f) E-$NiCo_2S_4$//AC ASCs at different current densities of 1–12 A g^{-1}.

scan rate of 10 mV s^{-1}, respectively. When the operation voltages increased to 1.8 V, a significant corner was observed in the CV curve of each ASC, which is due to the decomposition of the electrolyte.[44] Thus, we chose the working voltage of 1.6 V to further measure the electrochemical performance of the ASCs. Fig. 9c and d show the CV curves of optimized H/E-$NiCo_2S_4$//AC ASCs at different scan rates in the voltage window from 0 to 1.6 V. The CV curves reveal that the ASCs take advantage of both pseudocapacitive and electric double-layer capacitive performances due to the quasi-rectangular shape with distinct peaks. With the increase of the scan rate from 10 to 100 mV s^{-1}, no obvious distortion can be observed in the CV curves, indicating the fast charge–discharge reversibility and good rate capability of the ASCs. Furthermore, GCD curves of our ASCs at a series of current densities from 1 to 12 A g^{-1} are illustrated in Fig. 9e and f, which are used to evaluate the electrochemical performance and calculate the specific capacitance. As shown in Fig. S11c,† the specific capacitances of the H-$NiCo_2S_4$//AC ASC were calculated to be 100.06, 98.92, 72.94, 60.47 and 54.51 F g^{-1}, and the specific capacitances of the E-$NiCo_2S_4$//AC ASC were 79.44, 72.87, 68.97, 61.07 and 54.43 F g^{-1} at current densities of 1, 2, 4, 8 and 12 A g^{-1}, respectively. It is noteworthy that the specific capacitances of the H-$NiCo_2S_4$//AC and E-$NiCo_2S_4$//AC ASCs are retained at about 54.5% and 68.52% of the initial capacitances, respectively. These results indicate the good rate capability of the ACSs. The difference of the capacitances retention for two ASCs might be explained by the EIS tests as shown in Fig. S11d.† The E-$NiCo_2S_4$//AC ASC shows a lower minimized bulk resistance than the E-$NiCo_2S_4$//AC ASC in the high-frequency region, which hinders the excellent electrical conductivity and favorable fast charge-transfer kinetics of the ASCs at high current densities.

Fig. 10a shows the cycling stability of the H/E-$NiCo_2S_4$//AC ASCs under continuous charge–discharge tests at a constant current density of 10 A g^{-1}. The capacity retention of the H-$NiCo_2S_4$//AC ASC is 84.2% after 2000 cycles, demonstrating its excellent cycling stability. This is better than that of the E-$NiCo_2S_4$//AC ASC (69.2%). In the very low frequency region of the Nyquist plots in Fig. S11d,† the straight line with a larger slope demonstrates a lower charge-transfer resistance, which might exhibit better cycle stability without diffusion limitation in long-term charge–discharge measurements. Recent studies on developing high-energy density ASCs have made great progress, and it is of great significance to investigate the energy and power densities of ASCs for better practical applications.[47] The Ragone plots of the H/E-$NiCo_2S_4$//AC ASCs obtained from the charge–discharge measurements at different current densities are presented in Fig. 10b. It can be seen that the H-$NiCo_2S_4$//AC ASC achieves a maximum energy density of 35.6 W h kg^{-1} at a power density of 819.5 W kg^{-1}, and can still maintain an energy density of 19.4 W h kg^{-1} at a high power density of 11.3 kW kg^{-1}, while the energy density of the E-$NiCo_2S_4$//AC ASC decreases from 28.3 down to 19.4 W h kg^{-1} as the power density increases from 0.8 to 11.1 W kg^{-1}. These results are much better than those of other nickel cobalt sulfide-based asymmetric supercapacitors, such as $NiCo_2S_4$ nanotubes//RGO ASCs[48] (31.5 W h kg^{-1} at 156.6 W kg^{-1}), $NiCo_2S_4$

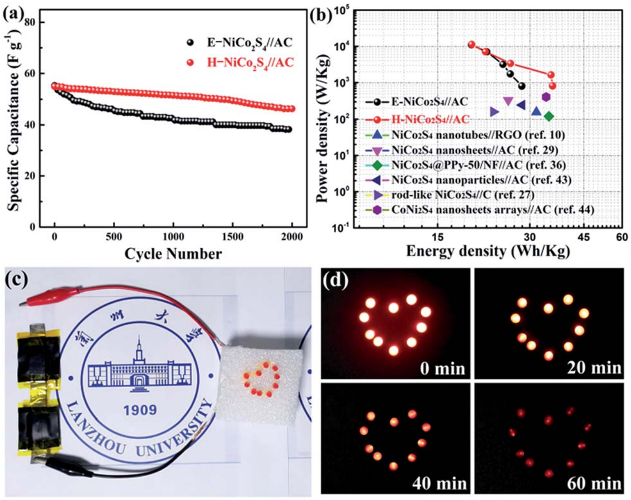

Fig. 10 (a) Cycling performance of the H-$NiCo_2S_4$//AC and E-$NiCo_2S_4$//AC ASCs during 5000 cycles at a constant current density of 10 A g^{-1}. (b) The Ragone plots related to energy and power densities of the H-$NiCo_2S_4$//AC and E-$NiCo_2S_4$//AC ASCs. (c) A photo of our H-$NiCo_2S_4$//AC and E-$NiCo_2S_4$//AC ASCs connected in series. (d) A "heart" design composed of ten LEDs (lowest working voltage of 2.03 V) was lit by using our H-$NiCo_2S_4$//AC and E-$NiCo_2S_4$//AC ASCs (charged to 2.1 V within 3 min) in series for around 1 h.

nanosheets//AC ASCs[31] (25.5 W h kg^{-1} at 334 W kg^{-1}), $NiCo_2S_4$@PPy-50/NF//AC ASCs[40] (34.62 W h kg^{-1} at 120.19 W kg^{-1}), $NiCo_2S_4$ nanoparticles//AC ASCs[49] (28.3 W h kg^{-1} at 245 W kg^{-1}), rod-like $NiCo_2S_4$//C ASCs[29] (22.8 W h kg^{-1} at 160 W kg^{-1}), $CoNi_2S_4$ nanosheets arrays//AC ASCs[50] (33.9 W h kg^{-1} at 409 W kg^{-1}). To demonstrate the practicability and operability of our ASCs, a combined device was prepared by connecting the H-$NiCo_2S_4$//AC ASC and E-$NiCo_2S_4$//AC ASC in series as shown in Fig. 10c. The two ASCs possess a voltage window of 1.6 V, and therefore the combined device can achieve a large voltage window of 3.2 V as expected, as described in Fig. S12.† The sharp peak of the GCD curve is similar to that of the single H/E-$NiCo_2S_4$//AC ASCs, implying that the combined device can easily power small electronics (working voltage is lower than 3.2 V). Impressively, the combined device can light a "heart" design composed of ten LEDs (2.03 V, 20 mA) for around 60 minutes after charging to 2.1 V within 3 minutes (Fig. 10d). All these attractive results further confirm the outstanding electrochemical performance and potential application of our ASCs.

4. Conclusions

$NiCo_2S_4$ nano-petals have been successfully synthesized by a hydrothermal method according to the process of flowers in full bloom. As electrodes for supercapacitors, such $NiCo_2S_4$ nano-petal electrodes deliver an ultrahigh specific capacitance of 2036.5 F g^{-1} at a current density of 1 A g^{-1}, superior rate capability (83.6% retention at a current density of 100 A g^{-1}) and remarkable cycle stability with a capacitance retention of 94.3% after 5000 cycles. Interconnected $NiCo_2S_4$ nano-petals with large diameters and ultrathin thickness can form a highly porous architecture, which is believed to benefit the electron transport at the electrode/electrolyte interface, leading to an excellent electrochemical performance. The as-fabricated asymmetric supercapacitors based on $NiCo_2S_4$ nano-petals//active carbon electrodes present a high energy density of at 35.6 W h kg^{-1} at a power density of 819.5 W kg^{-1}, with both high rate stabilities and excellent cycling stability. The practicability of our ASCs was successfully demonstrated by lighting up ten LED lights in series for 60 minutes.

Acknowledgements

This work was financially supported by the National Natural Science Foundation of China (No. 61376011).

References

1 C. Liu, F. Li, L. P. Ma and H. M. Cheng, *Adv. Mater.*, 2010, **22**, E28–E62.

2 J. Chang, Z. Gao, X. Wang, D. Wu, F. Xu, X. Wang, Y. Guo and K. Jiang, *Electrochim. Acta*, 2015, **157**, 290–298.

3 Y. Tang, S. Chen, S. Mu, T. Chen, Y. Qiao, S. Yu and F. Gao, *ACS Appl. Mater. Interfaces*, 2016, **8**, 9721–9732.

4 M. I. Hoffert, K. Caldeira, G. Benford, D. R. Criswell, C. Green, H. Herzog, A. K. Jain, H. S. Kheshgi, K. S. Lackner, L. J. Perkins, H. D. Lightfoot, W. Manheimer, J. C. Mankins, M. E. Mauel, L. J. Perkins, M. E. Schlesinger, T. Volk and T. M. L. Wigley, *Science*, 2002, **298**, 981–987.

5 J. R. Miller and P. Simon, *Science*, 2008, **321**, 651–652.

6 Z. Yu, B. Duong, D. Abbitt and J. Thomas, *Adv. Mater.*, 2013, **25**, 3302–3306.

7 J. Yan, Q. Wang, T. Wei and Z. Fan, *Adv. Energy Mater.*, 2014, **4**, 1300816.

8 P. Simon and Y. Gogotsi, *Nat. Mater.*, 2008, **7**, 845–854.

9 N. Jabeen, Q. Xia, S. V. Savilov, S. M. Aldoshin, Y. Yu and H. Xia, *ACS Appl. Mater. Interfaces*, 2016, **8**, 33732–33740.

10 N. Jabeen, Q. Xia, M. Yang and H. Xia, *ACS Appl. Mater. Interfaces*, 2016, **8**, 6093–6100.

11 L. Wang, Z. H. Dong, Z. G. Wang, F. X. Zhang and J. Jin, *Adv. Funct. Mater.*, 2013, **23**, 2758–2764.

12 L. Shen, L. Yu, X. Y. Yu, X. Zhang and X. W. Lou, *Angew. Chem., Int. Ed.*, 2015, **54**, 1868–1872.

13 J. Yang, C. Yu, X. Fan, C. Zhao and J. Qiu, *Adv. Funct. Mater.*, 2015, **25**, 2109–2116.

14 W. Fu, Y. Wang, W. Han, Z. Zhang, H. Zha and E. Xie, *J. Mater. Chem. A*, 2016, **4**, 173–182.

15 T. Qin, B. Liu, Y. Wen, Z. Wang, X. Jiang, Z. Wan, S. Peng, G. Cao and D. He, *J. Mater. Chem. A*, 2016, **4**, 9196–9203.

16 T. Qin, Z. Wan, Z. Wang, Y. Wen, M. Liu, S. Peng, D. He, J. Hou, F. Huang and G. Cao, *J. Power Sources*, 2016, **336**, 455–464.

17 G. Nagaraju, G. S. Raju, Y. H. Ko and J. S. Yu, *Nanoscale*, 2016, **8**, 812–825.

18 A. S. Arico, P. Bruce, B. Scrosati, J. M. Tarascon and W. Van Schalkwijk, *Nat. Mater.*, 2005, **4**, 366–377.

19 J. Jiang, Y. Li, J. Liu, X. Huang, C. Yuan and X. W. Lou, *Adv. Mater.*, 2012, **24**, 5166–5180.

20 W. Wei, X. Cui, W. Chen and D. G. Ivey, *Chem. Soc. Rev.*, 2011, **40**, 1697–1721.

21 P. J. Hall, M. Mirzaeian, S. I. Fletcher, F. B. Sillars, A. J. R. Rennie, G. O. Shitta-Bey, G. Wilson, A. Cruden and R. Carter, *Energy Environ. Sci.*, 2010, **3**, 1238.

22 Z. Yang, C.-Y. Chen and H.-T. Chang, *J. Power Sources*, 2011, **196**, 7874–7877.

23 L. Yu, B. Yang, Q. Liu, J. Liu, X. Wang, D. Song, J. Wang and X. Jing, *J. Electroanal. Chem.*, 2015, **739**, 156–163.

24 J. Wei, S. Xing, B. Yan, D. He, H. Suo and C. Zhao, *J. Mater. Sci.: Mater. Electron.*, 2015, **26**, 4185–4192.

25 J. Zhu, S. Tang, J. Wu, X. Shi, B. Zhu and X. Meng, *Adv. Energy Mater.*, 2016, 1601234.

26 L. Shen, Q. Che, H. Li and X. Zhang, *Adv. Funct. Mater.*, 2014, **24**, 2630–2637.

27 A. Sivanantham, P. Ganesan and S. Shanmugam, *Adv. Funct. Mater.*, 2016, **26**, 4661–4672.

28 J. Shen, P. Dong, R. Baines, X. Xu, Z. Zhang, P. M. Ajayan and M. Ye, *Chem. Commun.*, 2016, **52**, 9251–9254.

29 W. Kong, C. Lu, W. Zhang, J. Pu and Z. Wang, *J. Mater. Chem. A*, 2015, **3**, 12452–12460.

30 Y. Lu, Z. Zhang, X. Liu, W. Wang, T. Peng, P. Guo, H. Sun, H. Yan and Y. Luo, *CrystEngComm*, 2016, **18**, 7696–7706.

31 Z. Wu, X. Pu, X. Ji, Y. Zhu, M. Jing, Q. Chen and F. Jiao, *Electrochim. Acta*, 2015, **174**, 238–245.

32 L. Lin, J. Liu, T. Liu, J. Hao, K. Ji, R. Sun, W. Zeng and Z. Wang, *J. Mater. Chem. A*, 2015, **3**, 17652–17658.

33 J.-G. Wang, D. Jin, R. Zhou, C. Shen, K. Xie and B. Wei, *J. Power Sources*, 2016, **306**, 100–106.

34 F. Lu, M. Zhou, W. Li, Q. Weng, C. Li, Y. Xue, X. Jiang, X. Zeng, Y. Bando and D. Golberg, *Nano Energy*, 2016, **26**, 313–323.

35 P. Hao, J. Tian, Y. Sang, C. C. Tuan, G. Cui, X. Shi, C. P. Wong, B. Tang and H. Liu, *Nanoscale*, 2016, **8**, 16292–16301.

36 L. Shen, L. Yu, H. B. Wu, X. Y. Yu, X. Zhang and X. W. Lou, *Nat. Commun.*, 2015, **6**, 6694.

37 W. Chen, C. Xia and H. N. Alshareef, *ACS Nano*, 2014, **8**, 9531–9541.

38 T. Peng, H. Yi, P. Sun, Y. Jing, R. Wang, H. Wang and X. Wang, *J. Mater. Chem. A*, 2016, **4**, 8888–8897.

39 J. Yang, M. Ma, C. Sun, Y. Zhang, W. Huang and X. Dong, *J. Mater. Chem. A*, 2015, **3**, 1258–1264.

40 M. Yan, Y. Yao, J. Wen, L. Long, M. Kong, G. Zhang, X. Liao, G. Yin and Z. Huang, *ACS Appl. Mater. Interfaces*, 2016, **8**, 24525–24535.

41 V. H. Nguyen and J.-J. Shim, *Electrochim. Acta*, 2015, **166**, 302–309.

42 J. Yang, C. Yu, X. Fan, S. Liang, S. Li, H. Huang, Z. Ling, C. Hao and J. Qiu, *Energy Environ. Sci.*, 2016, **9**, 1299–1307.

43 X. Wu, S. Li, B. Wang, J. Liu and M. Yu, *New J. Chem.*, 2017, **41**, 115–125.

44 L. Shen, J. Wang, G. Xu, H. Li, H. Dou and X. Zhang, *Adv. Energy Mater.*, 2015, **5**, 1400977.

45 Y. Xu, X. Gao, W. Chu, Q. Li, T. Li, C. Liang and Z. Lin, *J. Mater. Chem. A*, 2016, **4**, 10248–10253.

46 Y. Wen, T. Qin, Z. Wang, X. Jiang, S. Peng, J. Zhang, J. Hou, F. Huang, D. He and G. Cao, *J. Alloys Compd.*, 2017, **699**, 126–135.

47 T. Zhai, L. M. Wan, S. Sun, Q. Chen, J. Sun, Q. Y. Xia and H. Xia, *Adv. Mater.*, 2017, **29**, 1604167.

48 H. Chen, J. Jiang, L. Zhang, D. Xia, Y. Zhao, D. Guo, T. Qi and H. Wan, *J. Power Sources*, 2014, **254**, 249–257.

49 Y. Zhu, Z. Wu, M. Jing, X. Yang, W. Song and X. Ji, *J. Power Sources*, 2015, **273**, 584–590.

50 W. Hu, R. Chen, W. Xie, L. Zou, N. Qin and D. Bao, *ACS Appl. Mater. Interfaces*, 2014, **6**, 19318–19326.